ACS Photonics

pubs.acs.org/journal/apchd5 Article

Unraveling the Nature of Lasing Emission from Hybrid Silicon Nitride and Colloidal Nanocrystal Photonic Crystals with Low Refractive Index Contrast

Published as part of ACS Photonics special issue "Rising Stars in Photonics".

Ivo Tanghe,* Tom Vandekerckhove, Margarita Samoli, Amelia Waters, Dulanjan Harankahage, Mikhail Zamkov, Zeger Hens, Christian Seassal, Hai-Son Nguyen, Dries Van Thourhout, and Pieter Geiregat*

Cite This: ACS Photonics 2024, 11, 4906−4915 Read Online

ACCESS | Metrics & More | Article Recommendations | Supporting Information

ABSTRACT: Silicon nitride is used for its low optical loss and high thermal stability, making it a suitable platform for visible-light applications in integrated photonic devices. However, its application has been limited due to inefficient light emission, a problem addressed by integrating various types of light emitters onto the platform. In particular, the integration of solution-processable colloidal nanocrystals (NCs) as optical gain materials onto the silicon nitride platform is a promising route but requires a more solid theoretical footing. By leveraging 2D surface-emitting photonic crystal structures combined with NCs, we effectively confine and manipulate light to achieve lasing from green to red. Building on this, we model the light−matter interactions of the low index contrast NC/nitride platform, validated by extensive experimental validations through Fourier imaging techniques, revealing the full photonic band structure and showing clear mode congestion. These comprehensive studies confirm the potential of hybrid NC-based structures for fully integrated on-chip laser applications and indicate routes for further improvement.

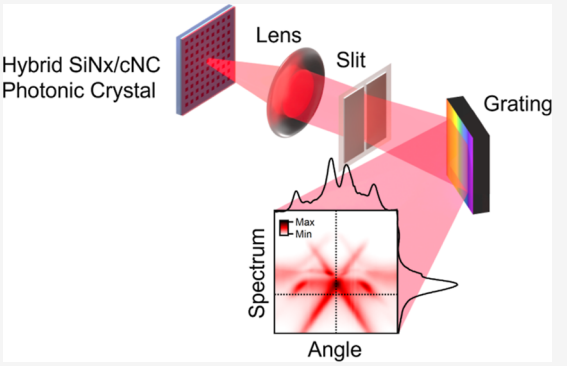

KEYWORDS: *photonic crystal, colloidal nanocrystal, laser, BIC lasing, silicon nitride, integrated photonics*

INTRODUCTION

The drive toward miniaturization in photonics implicates a need for compact, efficient, on-chip lasers capable of precise wavelength selectivity and directional emission. These devices are crucial across a variety of applications, including microdisplays, tunable light sources, and advanced sensing/imaging systems.[1,2] The need for integrating multiple laser sources on a single chip without compromising performance poses significant challenges in terms of possible device architectures and commensurate compatibility of the active materials.

Silicon photonics has emerged as a robust platform for addressing these challenges, particularly through the use of silicon nitride (SiNx), which offers excellent properties for visible-light applications due to its low optical loss in this part of the spectrum and a high thermal stability. By now, losses as low as 1 dB/m are achievable, allowing for quality factors (Q) above 1 million.[3] SiNx's compatibility with standard CMOS fabrication processes further enhances its appeal for integrated photonic devices.[4,5] However, despite its potential as a passive platform, the lack of efficient light emission from SiNx limits its wider application.

To address this, various heterogeneous integration methods have been developed to pair the low-loss SiNx platform with active semiconductor materials. These methods include bonding[6] and transfer printing,[7] which facilitate applications on the SiNx platform such as on-chip lasing with III−V semiconductors,[8] high-speed modulators, and efficient second-harmonic generation with lithium niobate.[9,10] However, these integration methods face clear limitations. For example, every additional bonding step requires complex processing, making it difficult to combine multiple gain materials on a single chip. Furthermore, both methods still require the use of two separate foundries to create both wafers, leading to a costly and complex manufacturing process.[2]

Received: July 30, 2024
Revised: October 24, 2024
Accepted: October 25, 2024
Published: November 1, 2024

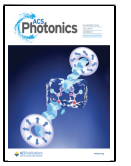

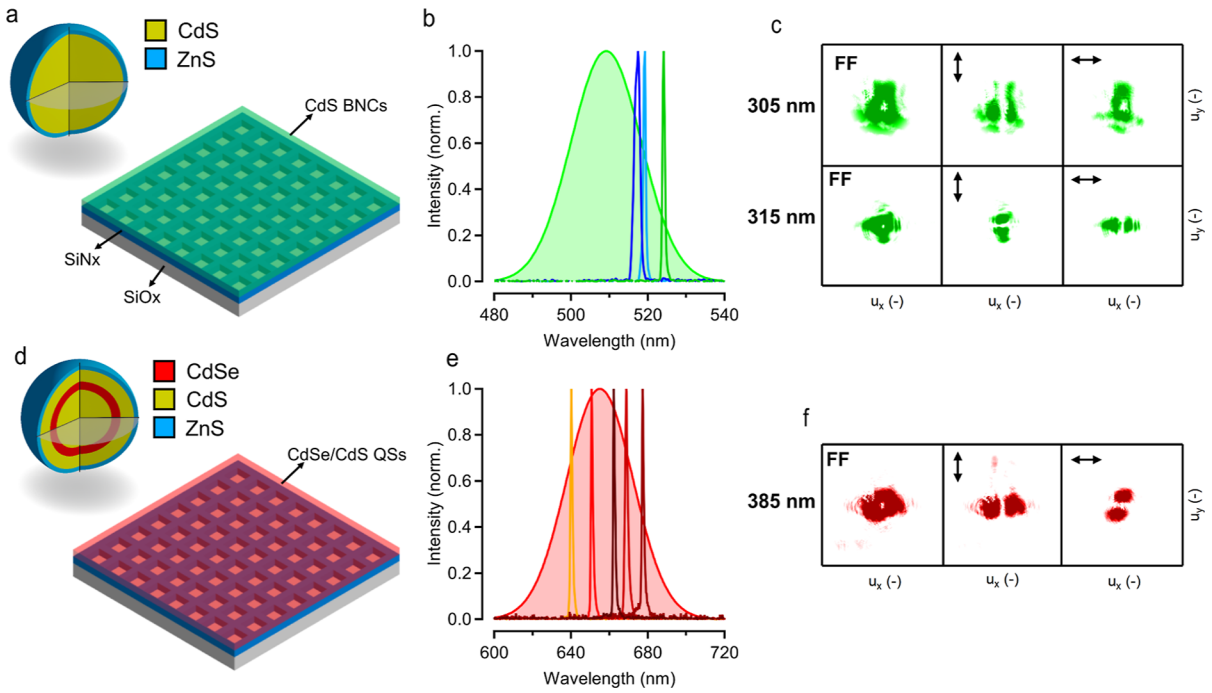

Figure 1. Lasing characteristics of hybrid colloidal NC/SiNx 2D PhC structures. (a) Schematic of a green emitting CdS BNC/SiNx device, with the inset showing a cross-section of a CdS BNC.[20] (b) PL spectrum of CdS BNCs (broad, green) overlaid with lasing peaks from devices with periods 300, 305, and 315 nm. (c) Unpolarized (left) and polarized far-fields of the 300 and 305 nm period device (top), compared to the 315 nm device (bottom). (d) Schematic of a CdSe/CdS QS/SiNx device, with the inset displaying a cross-section of a layered CdSe/CdS QS. (e) PL spectrum of CdSe/CdS QSs (broad, red) overlaid with lasing peaks from devices with periods between 385 and 405 nm. (f) Unpolarized (left) and polarized (middle and right) far-fields of the 385 nm device.

In this context, the integration of solution processable colloidal nanocrystals (NCs) onto SiNx presents a transformative approach for achieving the desired enhanced functionality. Indeed, NCs are obtained as an ink and hence are processable from a solution phase, allowing for cost-effective and straightforward methods for integration onto photonic chips, such as spin coating, Langmuir−Blodgett deposition, and/or inkjet printing.[11−13] Using their broadband and size-tunable absorption, demonstrations of on-chip photodetection have resulted in detection of on-chip light until 2100 nm.[14,15] Furthermore, NCs provide tunable emission wavelengths and can be engineered to exhibit high photoluminescence (PL) efficiency[16−18] combined with efficient optical gain metrics,[19−21] which is critical for the development of the highly desired on-chip laser sources mentioned above. Several demonstrations in the literature indicated the potential for lasing on the nitride platform, both in the green and red parts of the visible spectrum under quasi-CW optical excitation.[20−23] Also, electrically excited amplified spontaneous emission sources have been demonstrated.[24,25] In these demonstrations, a recent trend toward photonic crystal (PhC) cavities can be observed, both with one- and two-dimensional confinement, due to the ease of processing, as they consist of a single lithography step followed by depositing the active NC layer on top. These PhC surface emitting laser (PCSEL) implementations benefit from efficient collection of the collimated out-of-plane emission combined with efficient in-plane feedback, allowing for quick demonstrations of lasing in proof-of-concept experiments across the visible and near-infrared spectrum.[20,21,26−28]

In a broader context, PhC structures have already been extensively utilized to achieve spatially confined and highly efficient photonic devices, particularly in high-index contrast, epitaxially grown material systems.[29−31] These structures exemplify the ability to confine and manipulate light within very small volumes or to achieve very high output powers combined with directional and wavelength-selective light emission out-of-plane. Similar design techniques can be utilized on the SiNx platform combined with colloidal NCs. While such an approach clearly borrows from the mentioned high-index contrast systems, the inherent low refractive index of SiNx ($n \approx 2.0$) lines up with that of most NC composite films ($n \approx 1.8-2.2$),[27] leading to a low index contrast system. The latter should lead to differences in the light−matter interactions, such as mode congestion, but this has not been verified experimentally.[32] Indeed, whereas PhC-based laser structures combined with NCs have been presented in the past, they are typically not explored in-depth from a purely photonic perspective and more used as a means to an end.[26−28] Due to an absence of experimentally validated theoretical modeling of these hybrid NC/PhC structures, it thus remains rather unclear at the moment what the possible (dis)advantages are of the low index contrast NC-PhC cavities used extensively in the literature and, importantly, how we can exploit and/or mitigate these further toward scalable NC-enabled laser technology.

In this work, we first demonstrate and characterize lasing from SiNx PhC devices coated with thin layers of NCs, thereby using two state-of-art colloidal gain materials: red-emitting CdSe/CdS quantum shells (QSs)[21,33,34] and green-emitting CdS bulk NCs (BNCs).[20] Both materials were spin coated from a colloidal dispersion on similar SiNx chips, underscoring the versatility of the hybridization approach. Next, we take one step back and develop the theory behind these hybrid devices by simulating the photonic band structures of the low refractive index contrast

https://doi.org/10.1021/acsphotonics.4c01410
ACS Photonics 2024, 11, 4906−4915

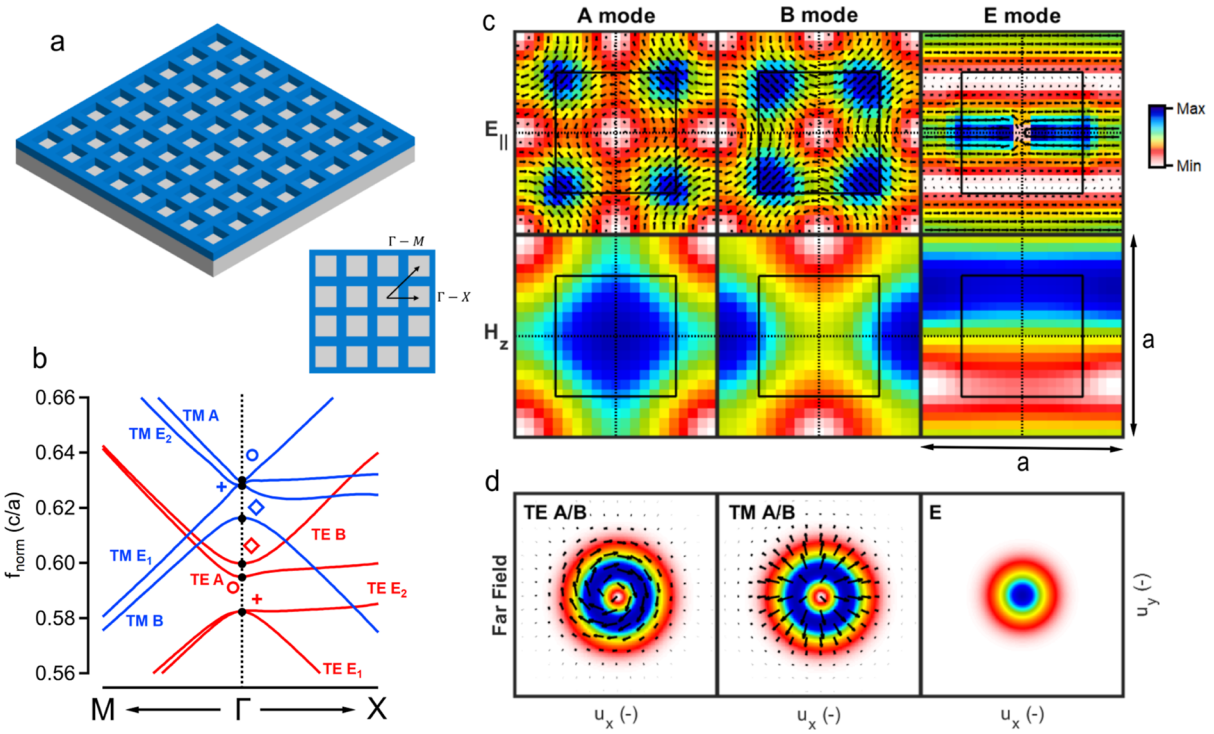

Figure 2. Photonic band structure, mode profiles at Γ and far-field patterns. (a) Schematic of a PhC layer on SiNx on top of SiOx. (b) PhC band diagram around Γ, where 10% of the way to the *M*- and *X*-points are shown. Modes are labeled according to typically used nomenclature. (c) Transverse electric (TE) mode field profiles for all three mode types at the Γ-point. In-plane electric fields are shown in the top row, and out-of-plane magnetic fields are shown in the bottom row. Other field components are zero. For transverse magnetic (TM) modes, the field profiles are reversed, where there exist only in-plane magnetic field components and out-of-plane electric field components. (d) Theoretical far-field ring-shaped patterns for TE and TM *A*/*B* modes, displaying the azimuthal and radial polarization, respectively. Far-field pattern for the *E*-mode is also shown to be Gaussian. Size of the rings and Gaussians depends on the amount of periods in a structure.

SiNx/NC systems by using the finite element method (FEM). The simulations allow us to identify and catalog the various possible modes and their energy dispersion.[35] To validate our theoretical models, we proceed to employ 2D Fourier imaging[36] to directly measure the photonic band structure of the devices. These measurements were conducted on both bare SiNx PhC structures and structures integrated with NCs, capturing for the latter both their reflection and PL behavior. From these measurements, we deduce unambiguously the photonic bands with which the NC emission-optical gain interacts. Our experimental results not only confirm the theoretical predictions concerning the lasing mechanisms and mode families in the low index contrast PhC structures but also highlight the potential of these structures for further applications, where they can be used not only as resonators for lasing and strong coupling but also to enhance emission for LEDs or single-photon emitters. With this thorough understanding available, targeted design for any of these applications is within reach.

LASING FROM COLLOIDAL NC/SINX 2D PHC DEVICES

PhC devices are fabricated on a SiNx-on-SiOx platform, where periodically etched holes with a designed 60% duty cycle are etched into a 170 nm thick SiNx layer with periods ranging from 300 to 425 nm, in increments of 5 nm, designed to tune the photonic band structure, where increasing the period will red-shift the bands. Following the etching process, NCs are spin-coated from solution onto the devices under ambient conditions. This typically fills the etched holes and forms an overcoat of approximately 50 nm thick; see Methods. In this work, we prepared three distinct chip variants with a relevant period sweep for experimental analysis: a bare structure without NCs, one incorporating CdS BNCs[20] (Figure 1a−c), and another with CdSe/CdS QSs[21] (Figure 1d−f). The periods range from 300−380 nm for the bare SiNx chip, 300−340 nm for the BNC/SiNx chip, and 385−425 nm for the QS/SiNx chip. Figure 1a,d shows schematics of a device emitting green and red light, respectively, and the insets depict a schematic of the NC material's core/shell architecture. The PL and lasing peaks for these materials are illustrated in Figure 1b,e. For the green chip, PL ranges from 490 to 530 nm, with lasing observed between 515 and 525 nm. The green-emitting colloidal NCs used here are CdS NCs with a diameter of around 12 nm, larger than the Bohr-radius. As such, they behave optically like bulk CdS, as studied before.[20] The red chip shows PL from 630 to 680 nm, with a lasing range of 640 to 680 nm. The red-emitting colloidal NCs are large CdS core QSs, where the carriers are mainly confined within the first shell of CdSe.[21] Their total diameter is about 21 nm. The observed spectral bandwidth over which lasing is obtained is in line with previous reports,[20,21] beit slightly narrower due to the more restricted PhC lattice period sweep used in this study. A more detailed line width and threshold behavior analysis of the lasers is shown in Supporting Information, Section S2.

Additionally, Figure 1c,f includes an analysis of the polarized and unpolarized far-field patterns for multiple devices, which are crucial for assessing the specific optical mode that is resonating. All patterns exhibit a typical ring-shaped far-field pattern for these types of structures. For the green-emitting devices, both smaller periods (300 and 305 nm) exhibit the same far-field

https://doi.org/10.1021/acsphotonics.4c01410
ACS Photonics 2024, 11, 4906−4915

patterns, shown in Figure 1c (top), with two horizontal (vertical) lobes when vertically (horizontally) polarized. The device with the larger period (315 nm), however, displays the inverse: horizontal (vertical) lobes when horizontally (vertically) polarized, as shown at the bottom of the same figure. The red-emitting devices consistently show similar far-field patterns across all devices that exhibit lasing, as depicted in Figure 1f. The same ring-shaped far-field pattern is seen, where the polarized measurements display behavior similar to that of the shorter period green devices.

MODELING 2D PHC BAND STRUCTURES AND OPTICAL MODES

In this study, we investigate devices characterized by square-like periodicity across two dimensions, as shown in Figure 2a. Light is confined within these two dimensions (in-plane) and only confined due to the index contrast in the third dimension, which is perpendicular (out-of-plane). Typically, such devices are described through second order Bragg diffraction, described by the equation $m\cdot\lambda = 2n_{\text{eff}}\Lambda$, where $m = 2$ corresponds to second-order diffraction. This configuration allows for both perpendicular (out-of-plane, 90°) and backward (in-plane, 180°) scattering. The combination of both in-plane and out-of-plane scattering is crucial for device operation: in-plane scattering is necessary for confinement, whereas out-of-plane scattering enables surface emission.

By solving Maxwell's equations for these devices using FEM, we find eight possible optical (eigen) modes, each with a distinct polarization and spatial symmetry. These modes' field profiles can be catalogued into two groups: TE modes, which have only in-plane electric field components and an out-of-plane magnetic field component, and TM modes, where the field distributions between electric and magnetic components are swapped compared to TE. The presence of these modes at distinct wavelengths stems from their different field profiles present in each material of the device, known as geometric dispersion.

The modes are also categorized based on the symmetry of their out-of-plane components.[35] With square-like symmetry, this system belongs to the C_4 point group, and therefore so will the optical modes that are the solutions. The mode invariant under all symmetry operations is labeled as the *A*-mode. The mode that inverts under 90° or 270° rotation and remains constant for the other operations is the *B*-mode. The other two modes, E_1 and E_2, are degenerate and span a space where symmetry operations transform their field distributions into linear combinations of both. Both the TE and TM modes share this out-of-plane field distribution except that *E*- and *H*-fields are swapped. This symmetry-centric approach provides a comprehensive understanding of the optical behavior within these structured fields. The various field profiles for a single period are displayed in Figure 2c, specifically for TE modes. Only one of the *E*-modes is displayed, and the other solution is the same yet rotated over 90°.

The symmetry of the optical mode heavily influences the emission properties of the structure. For the *A*- and *B*-mode, the in-plane fields are antisymmetric with respect to the *x*- and *y*-axes, leading to destructive interference for upward scattered light. This interference nullifies the amplitude of this component, effectively confining the light completely within the plane. This phenomenon is crucial for the high quality performance of on-chip lasers, such as PCSELs,[37] and for describing specific optical modes, namely, (quasi-) bound in continuum (BIC) modes, which can lead to lasing.[38,39] Theoretically, the *A*- and *B*-modes in an infinite device will not display any surface emission, which is not the case for our finite size of devices. This leads to out-of-plane emission with a finite quality (Q) factor. The *E*-mode lacks this antisymmetry, allowing light to escape the cavity and emit perpendicular to the plane, which enhances emission or reflection for that specific mode and results in lower Q. This underscores the importance of understanding how design choices influence relative wavelength positions within a structure.

Deviations from perpendicular Bragg diffraction will result in different modes than those given above and in the emergence of modes within the structure that possess specific in-plane wave vector ($k_{\parallel}$) values, forming distinct photonic bands. The magnitude of $k_{\parallel}$ directly influences the emission angle associated with each photonic band and wavelength. By employing FEM, the eigenmodes of the system for specific boundary conditions—set by choosing a value for $k_{\parallel}$ within the Brillouin zone—can be determined from which photonic bands can be constructed, as shown in Figure 2b. Here, the *x*-axis represents the wave vector path typically moving from the *M*-point, through the Γ-point, to the *X*-point within the Brillouin zone, following the path shown in the inset. These points correspond to wave vector values of $\left(\frac{\pi}{a}, \frac{\pi}{a}\right)$, (0,0), and $\left(\frac{\pi}{a}, 0\right)$, respectively, where a is the period. The plot zooms in on approximately 10% of the region toward the *M* and *X* points, as optical modes around Γ are the main interest here, as we are looking into surface emission.

The photonic band structure and the field profiles shown apply to devices that extend infinitely. However, in finite and realistically processed devices, this antisymmetry is disrupted close toward the edges, which allows for upward emission from the *A*- and *B*-modes, albeit at a specific, small angle-dependent on the overall size of the structure. In larger structures, this emission intensity diminishes, and the emission angle narrows. In contrast, the *E*-mode's emission resembles a Gaussian distribution, where the width is determined by the number of periods in the structure. This results in either a ring-shaped (for *A* or *B*) or Gaussian (for *E*) far-field pattern, which can be used experimentally to discern whether the emission originates from the *A*/*B*-modes or from the *E*-mode. Additionally, the polarization of the emitted ring indicates whether the mode is TE or TM. The rings are azimuthally and radially polarized, respectively, and are displayed in Figure 2d. By employing a polarizer, it is possible to differentiate between these two modal polarizations. For TE rings, lobes will appear perpendicular to the polarization axis, whereas for TM lobes they appear parallel. This is demonstrated in Figure S2 in the Supporting Information.

As previously mentioned, the field distributions in the different materials determine the positions of the modes at Γ. This is influenced by both the absolute value of the effective index and the contrast between the refractive indices. Typical values for Cd-based colloidal NC are $n = 1.8-2.2$, whereas the SiNx used has $n = 2.0$ in the visible spectrum. The low index contrast of $\Delta n \approx 0.2$ between the materials will bring the various optical modes closer together. Due to the low index contrast in colloidal NC/SiNx PhC structures, all six optical modes are typically 30−40 nm spaced apart only, a point we will come back to further on in the discussion and Figure 6.

https://doi.org/10.1021/acsphotonics.4c01410
ACS Photonics 2024, 11, 4906−4915

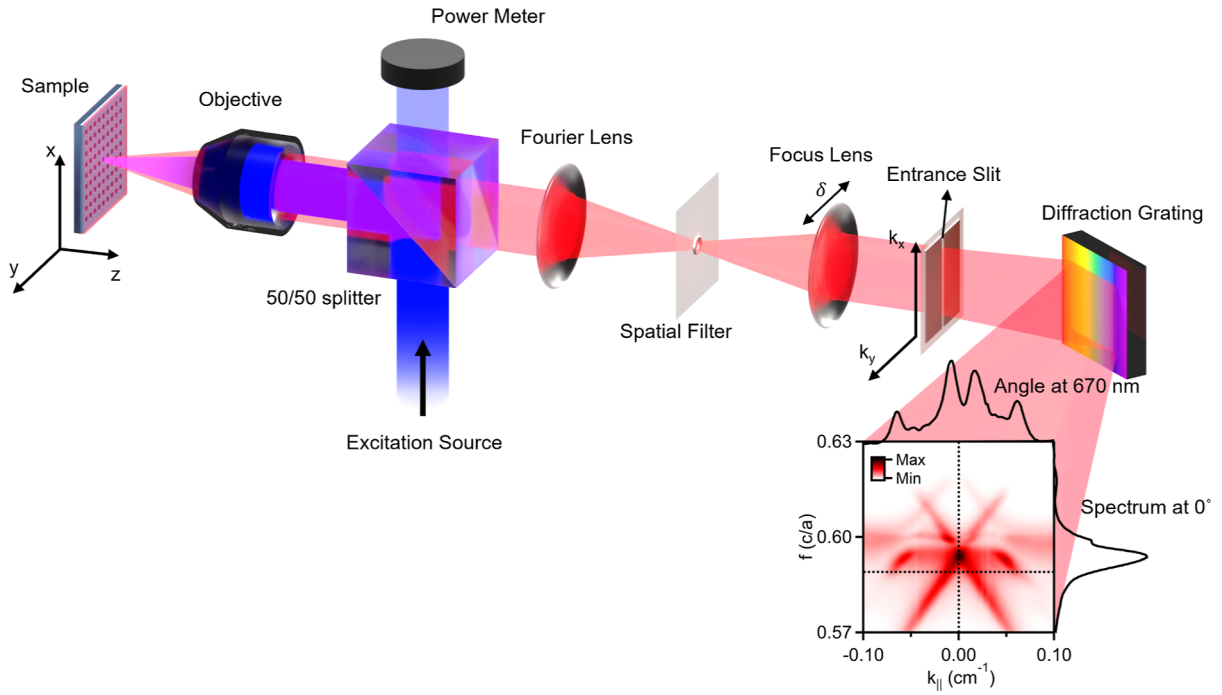

Figure 3. 2D Fourier imaging setup sketch. Example measurement is shown with a 2D NC/SiNx PhC device being excited with blue light, focused on the sample through an objective. Emission is collimated, filtered, and diffracted by a grating to find the energy−momentum map. Map shown is for a QS/SiNx device with a period of 390 nm.

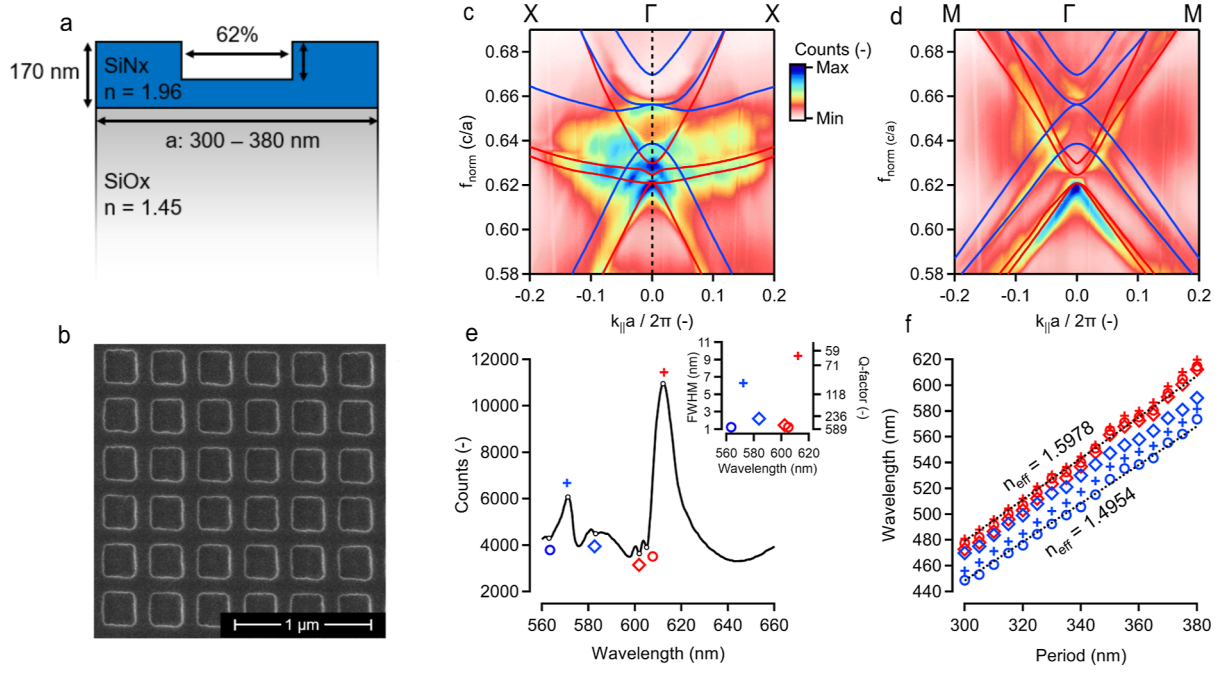

Figure 4. 2D Fourier imaging on bare SiNx PhC structures using reflection. (a) Cross-section of device with various parameters as used to find photonic band structures with FEM. (b) Top-view of a structure with a period of 350 nm, as measured with SEM. (c) *X*−Γ−*X* energy−momentum dispersion map of a structure with a period of 335 nm. TE bands (red) and TM bands (blue) are found through FEM. (d) *M*−Γ−*M* energy−momentum dispersion map of a structure with a period of 335 nm. (e) Spectrum taken at an emission of 0°, with the six resonances denoted by the symbols. Inset displays the fwhm of these resonances, showing the much broader features for the *E*-modes compared to *A*/*B*, indicating the higher degree of loss in these particular modes. (f) Determined positions of all six modes for all periods. Expected linear relationship between period and wavelength is found, with a reasonable value for the effective index range for a SiNx/air clad structure.

2D FOURIER IMAGING

Having set the theoretical framework for hybrid NC/PhC devices, we proceeded with an in-depth experimental analysis to verify its validity. To this end, we employ well-established 2D Fourier imaging techniques,[36,40−42] which involve projecting a Fourier image onto the diffraction grating of a spectrometer equipped with a CCD-camera, see Figure 3. Such a setup allows determination of the photon energy−momentum dispersion

https://doi.org/10.1021/acsphotonics.4c01410
ACS Photonics 2024, 11, 4906−4915

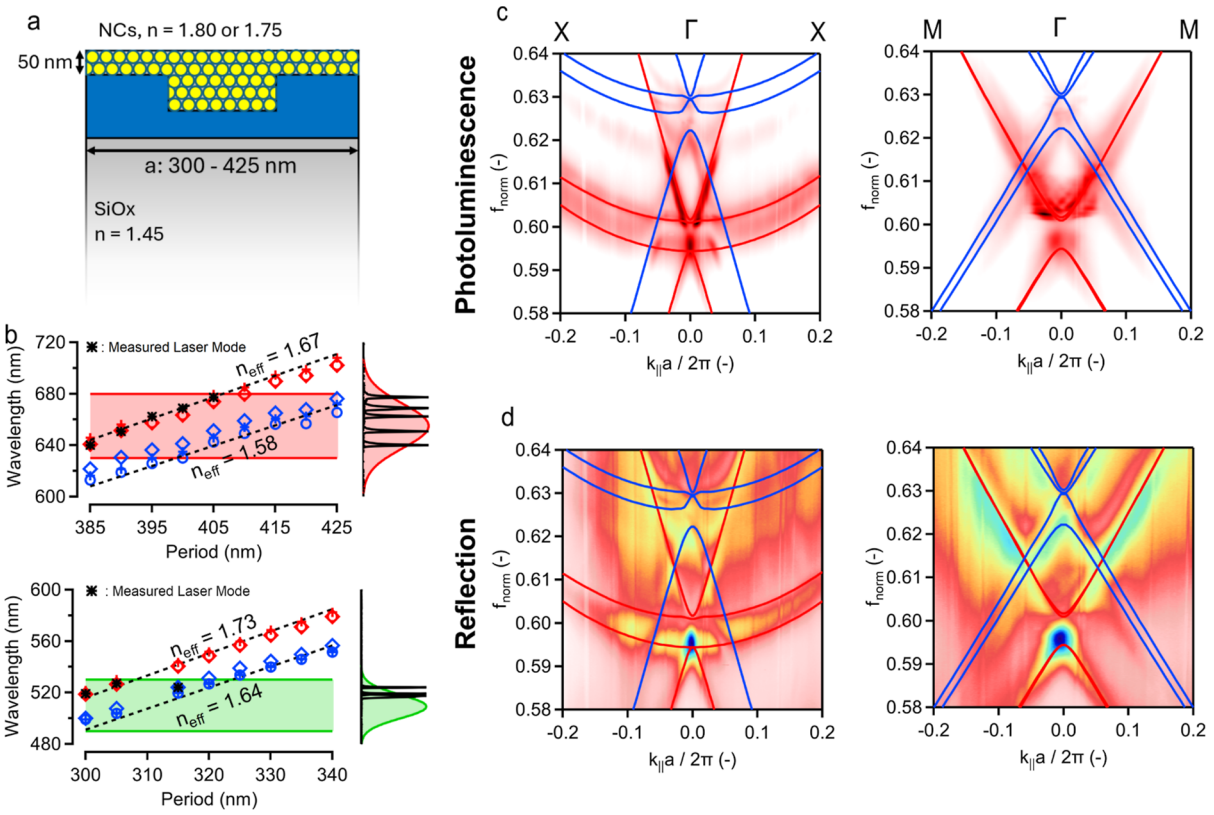

Figure 5. 2D Fourier imaging on NC/SiNx PhC structures. (a) Cross-section of a NC/SiNx device, with the parameters indicated as used to find photonic band structures with FEM. (b) Measured resonances for all measured periods for both the QS (red emitting, top) and BNC (green emitting, bottom)-based devices. Expected linear relationship between period and resonant wavelength is found experimentally and shown by the dashed black lines. The black asterisks indicate the spectral position of the measured lasing peaks, showing overlap with TE modes except for the device with a period of 315 nm. The right side displays the PL spectrum of the NCs and the various laser peaks imposed for reference. (c) Energy−momentum maps for X−Γ−X and M−Γ−M when measuring PL at a period of 395 nm. (d) Same as (c) but when measuring reflection.

characteristics of the devices under study. Through these measurements, more information can be gathered than by checking the far-field pattern above the threshold, as here all photonic bands can be determined together with their dispersion relationship moving away from the Γ-point. Indeed, when lasing action kicks in, all information is lost on these modal dispersion details as the energy collapses onto the mode that experiences the highest gain.

The excitation source first passes through a splitter, using either white light to measure reflection, or an excitation source, typically a blue (450 nm) pump laser, to induce light emission from the NC layer and is then focused using an objective lens. The reflected light or the PL is then collected through the same objective and passes through the splitter through the Fourier lens, which will focus on a spatial filter to make sure only emission from a small area is collected. Following this, the focus lens again collimated the beam and projected the Fourier image onto the slit of the spectrometer. For this particular setup, one momentum axis is preserved for light reaching the slit, while only the component with zero momentum is allowed to pass in the perpendicular direction. This selection is carefully controlled by adjusting the position of the focusing lens, as given in Figure 3 by δ. The zero in-plane momentum component is then dispersed by the diffraction grating, transforming this axis into an energy or wavelength axis. This results in a 2D map that displays counts as a function of one component of the in-plane momentum and as a function of the wavelength or energy, allowing us to check both the spectrum at specific emitted angles and the emitted angles for a specific wavelength or energy. When the structure is aligned parallel to the slit of the spectrometer, a measurement along the X−Γ−X direction can be performed. Rotating the sample is rotated under 45°; the M−Γ−M direction is probed.

The results from such measurements are typically displayed as normalized to the period. Here, f_{norm} is defined as $f \times \frac{a}{c}$. The wave vector, which is limited by the numerical aperture of the objective lens and the size of the CCD, is mapped to the normalized wave vector by multiplying with the period and dividing by 2π, resulting in $\frac{k_{||}a}{2\pi}$. For the M−Γ−M direction, an additional correction factor of $\sqrt{2}$ is necessary as we are looking at $k_x + k_y$. Through this normalization, a value of 0.5 corresponds to the edge of the Brillouin zone. In what follows, these measurements are always combined with FEM simulations to determine photonic band structures, where typically very good overlap is found.

RESULTS

Bare SiNx Structures. First, 2D Fourier imaging is applied to bare SiNx-on-SiOx PhC devices, as shown in Figure 4. As there are no emitters present, only the reflection of a broadband source can be measured. A cross-section of a device, together with the simulation parameters, based on design and scanning electron microscopy images (SEM), is shown in Figure 4, displaying a partially etched-through SiNx periodic structure with a total height of 170 nm (blue). In Figure 4b, a top-view SEM image is shown of a device with a period of 350 nm. Figure

https://doi.org/10.1021/acsphotonics.4c01410
ACS Photonics 2024, 11, 4906−4915

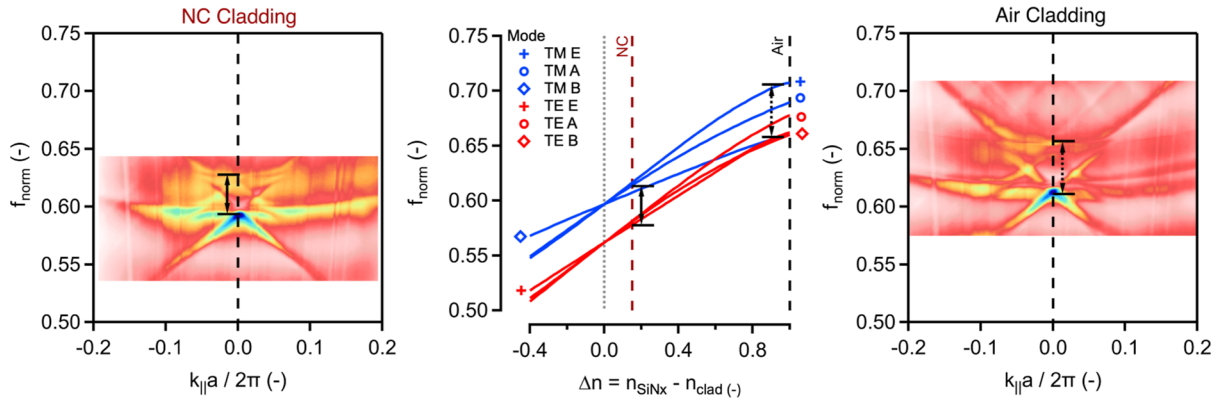

Figure 6. Comparison of experimentally found and simulated mode separation. Left and right images display measured band structures through reflection for a NC-clad or air-clad SiNx PhC. This is compared to simulated found resonances at the Γ-point in the middle when changing the refractive index of the cladding. Separation of the modes is noticeably smaller for the NC-clad device as expected from theory.

4c,d displays energy−momentum maps $X-\Gamma-X$ and $M-\Gamma-M$, with the simulated photonic bands overlaid on top, where bands marked in red (blue) denote TE (TM) bands. Figure 4e shows a reflection spectrum taken at 0°, as displayed by the vertical dashed line in Figure 4e, showing various peaks and dips that can be related to the different optical modes. The *E*-modes exhibit enhanced reflection, as light is efficiently being coupled out perpendicular to the chip surface, in contrast to the *A*/*B*-modes that display lower reflection, resulting in a dip in the reflection spectrum. Extracting the widths of these peaks, as displayed in the inset, shows that the resonances occurring for the *A*/*B*-modes are almost an order of magnitude sharper compared to the *E*-modes due to their antisymmetric field profiles and resulting forbidden upward scattering. The quality (Q)-factors are inversely proportional to the peak width and are most likely limited by processing variations of the different periods across the device/chip. Finally, in Figure 4f, the different wavelengths of the modes are extracted for all performed measurements, demonstrating the expected red-shifting of the resonance when increasing the period combined with consistent positioning of all different optical modes at Γ. For the shortest and longest wavelength modes, the effective index is furthermore found from a linear fit, yielding values between 1.5 and 1.6, an expected value for a SiNx (n = 2.0) structure that is air-clad (n = 1). The reflection energy−momentum maps for other air-clad devices can be seen in Figure S3 in Supporting Information, Section S4.1 for reference.

Coated Structures. Moving to CdSe/CdS QS/SiNx devices active in the red part of the spectrum first, similar 2D Fourier imaging is performed for devices ranging from 385−425 nm. A cross-sectional sketch of a period is shown in Figure 5a, with various parameters used in the FEM simulation. A refractive index of 1.8 is used for the red emitting QSs, and a typical value used for colloidal NC films.[27] The measured resonances for all devices are shown in Figure 5b on top (red coloring), overlaid with the measured lasing mode for all devices, indicating all the lasing occurs at TE modes, confirming the earlier far-field measurements. The PL band is also displayed, ranging from 630−680 nm (Gaussian shape, flipped 90°). Interestingly, there is no lasing for longer periods where a shift back to shorter wavelengths is observed, similar to previously reported results.[21] For longer periods, lasing originating from TM modes is expected, as there is better overlap with the gain band, the shaded area in Figure 5b (top), and these modes. In Figure 5c, the PL energy−momentum maps for $X-\Gamma-X$ and $M-\Gamma-M$ are displayed for the 395 nm period structure. Figure 5d displays the same two maps, but for reflection. Both of these show good overlap with the simulated photonic bands. For this specific period, the PL overlaps mainly with the TE bands (which can be seen in Figure 5b) and from the PL energy−momentum map. Clearly, an increase in reflection can be seen at the *E*-mode, while a dip is present at the *A*/*B*-modes. More energy−momentum maps can be seen in Figure S4 and in Supporting Information, Section S4.2.

Finally, similar measurements are also done for CdS BNC/SiNx devices in the green spectral window. The found resonances are displayed in Figure 5b (bottom), and the energy−momentum maps are shown in Figure S5. Here, as shorter wavelengths are of interest and the BNCs have a similar refractive index to the red, as both are composed mainly of Cd-chalcogenide material, the device periods are shorter compared to the red spectrum and range from 300 to 340 nm. A refractive index of 1.75 is used for the BNCs to achieve a good match with the experiment. As the CdS BNCs are smaller than the QSs (12 nm diameter vs 21 nm), a lower percentage of space is being occupied by BNCs compared to QSs, which most likely results in a slightly lower effective refractive index of the coating layer. The found resonances for all devices are shown in Figure 5b (bottom), overlaid with the measured lasing mode for all devices, showing lasing from both TE and TM, in accordance with the far-fields, as displayed in Figure 1c. The PL band is again indicated flipped on the right, now ranging from 490−530 nm. The jump back to shorter wavelengths noticed for the 315 nm device nicely overlaps with the TM *B*-mode found from 2D Fourier imaging, serving as additional proof for our characterization. In Figure S6a, PL energy−momentum maps for $X-\Gamma-X$ and $M-\Gamma-M$ are displayed when exciting with the same blue laser source as that for the QS sample. Figure S6b displays the same two maps, but a reflection experiment is shown. Here, clearly an increase in reflection can be seen at the *E*-mode, while a dip is present at the *A*/*B*-modes, for TE polarization. Noticeably more light couples into TM modes when going toward larger periods, as can be seen from Figure S5 from the Supporting Information, Section S4.3.

DISCUSSION AND OUTLOOK

As expected from PhC theory, the refractive index contrast Δn between the 2D SiNx grating and any cladding material dictates the resulting mode spacing. The central tab of Figure 6 shows such a theoretical prediction where a SiNx (fixed n = 2.0) PhC is

https://doi.org/10.1021/acsphotonics.4c01410
ACS Photonics 2024, 11, 4906−4915

coated with a changing cladding index, resulting in a sweep of the index contrast from −0.4 to +1.0. The NC films used in this work are situated around $\Delta n = 0.2$, where a clear congestion of the modes is observed compared to the air-clad case around $\Delta n = 1.0$, see also vertical dash lines in Figure 6 (middle). Experimental confirmation of this prediction is found by taking a look at the results of Figures 4 and 5 for the bare and coated cases studied in detail. Summarizing these results in Figure 6 on the left for NC cladding and on the right for air cladding, we indeed confirm that the clustering of modes is experimentally present for the NC coated case. In particular, this can be seen in the spread Δf visualized by the vertical black lines in the $f(k)$ maps, which are reproduced on the $f(\Delta n)$ central figure. As a result, the PL, and eventually lasing, tends to couple with multiple bands within a single device, which would impede single-mode operation. Several design choices, i.e., ranging from duty cycle adjustments to more complex patterns in the unit cell, have been shown with epitaxial growth approaches to impact the mode positioning and should be explored in further work toward more robust single mode operation.[31,43] If however single mode character is not required, one could of course proceed with existing architectures. Embedding the NC layer and defining a grating in the top nitride layer could also improve the index contrast further, but requires layer deposition onto the NC film, an approach shown to be viable in earlier works.[23]

We further note that, whereas high index contrast approaches are easier to push to single mode operation, they typically rely on a remote gain section separated from the PhC region.[30] Such an approach reduces the overlap of the gain medium with the feedback of the PhC structure, where in our hybrid devices the gain layer is an intrinsic part of the PhC, which improves the modal gain and could lead to more compact devices and/or higher output power devices in the future.

Finally, as shown in the inset of Figure 4e, we should note that the Q-factors we observed (60−600) for the bare nitride cavities are significantly lower than those reported for other PhC structures based on epitaxially grown material systems or state-of-art SiNx fabrication.[3,44] It stands to reason that further improvements in the SiNx inherent optical quality, combined with improved etching and lithography, should hence allow making high Q-factor cavities based on SiNx over a spectrally very broad window, a clear-cut road ahead for future work. We note that also the roughness of the NC coating can play a role, where indeed prior studies on colloidal NC/SiNx disk lasers have shown Q-factors of up to 5000 by embedding NCs into the nitride stack instead of using a top-coating as used in this work.[23]

CONCLUSIONS

In this study, we provided a solid and comprehensive experimental verification of the light−matter interactions between SiNx-based 2D PhC structures and colloidal NCs as a light-emitting and amplifying medium. In particular, the theoretically predicted mode congestion feature of low index contrast systems was clearly experimentally verified in the tendency to bunch optical modes within a narrow spectral bandwidth, posing challenges for achieving single-mode operation in lasing devices. Whereas several routes can be explored to lift this problem, it must be said that not all laser applications necessitate single-mode operation and that the inherent qualities of the SiNx platform, especially its low loss and wide spectral range, most likely will offset these inherent limitations in future applications.

METHODS

NC Synthesis. NC samples were synthesized according to previous work in Tanghe et al.[20] (CdS BNCs) and Tanghe et al.[21] (CdSe/CdS QSs). For more details, see Supporting Information, Section S1.

PhC Cavity Fabrication. Silicon substrates with 1 μm silicon oxide are used as the starting chip. These are first cleaned using acetone and isopropanol, followed by an oxygen plasma treatment. By plasma-enhanced chemical vapor deposition, 170 nm of SiNx is deposited at 270 °C. To create the grating, electron beam lithography is used. First, the positive resist AR-P 6200.13 is used, spin-coated at 4000 rpm, to achieve resist thicknesses of 400 nm. The chip is then baked at 150 °C for 60 s. After this, AR-PC 5090 is spun as a protective coating, also at 4000 rpm, to achieve a layer around 40 nm thick. This conductive coating increases the electron beam lithography resolution. After spin-coating, the chip is baked at 90 °C for 120 s. E-beam lithography is done using a Raith Voyager system, using a dose of 160 μC/cm^2. After exposure, the chip is developed by putting it into a bath of n-amyl-acetate for 60 s, following an isopropanol bath for 60 s. A specifically optimized reactive ion etching process based on a CF_4/H_2 chemistry is used to etch the SiNx layer and is about halfway etched through. After the etch, the remaining resist is cleaned off using an oxygen plasma treatment. Finally, the NCs are spin-coated on top, giving a thickness around 45 nm.

2D Fourier Imaging. The reflection energy−momentum maps are measured with a collimated white light source spanning the entire visible spectrum. For PL, an LDH-P-C-405 excitation laser from Picoquant is used. This laser operates at 405 nm with pulses of ≈50 ps, at a repetition rate of 80 MHz. As a spectrometer, the microHR spectrometer from Horiba is used in combination with the CCD Syncerity camera for detection.

Laser Measurements. For the laser measurements, samples were excited using 190 fs pump pulses at 450 nm, generated starting from 1030 nm through nonlinear interactions in an optical parametric amplifier. The beam is reflected on a dichroic mirror with a cutoff wavelength of 488 nm and is then focused perpendicular on the sample. The surface emission is transmitted through the dichroic. Following this, a 50/50 splitter is used, where 50% of the light is focused on a fiber for spectral analysis and 50% is focused on a camera for imaging. The fiber went to an Andor Shamrock 750 Spectrograph.

PhC Simulations. A geometry is used, as shown in Figure 4a (SiNx only) and Figure 5a (QS/SiNx). A full 3D simulation is done with in-plane Bloch boundaries (x- and y-direction). The out-of-plane direction has a perfectly matched layer as a boundary; at the top, this is situated in air; at the bottom, it is located within the SiOx. Through FEM, the eigenvalues of the structure are found. In-plane fields are inspected to find the specific relevant mode. By changing the Bloch boundary to include a phase shift, the simulation can be repeated and the full band structure is determined.

ASSOCIATED CONTENT

Supporting Information

The Supporting Information is available free of charge at https://pubs.acs.org/doi/10.1021/acsphotonics.4c01410.

NC synthesis, extra information regarding the polarized far field maps, and additional measured energy−momentum maps (PDF)

https://doi.org/10.1021/acsphotonics.4c01410
ACS Photonics 2024, 11, 4906−4915

AUTHOR INFORMATION

Corresponding Authors

Ivo Tanghe − *Photonics Research Group, Ghent University, Gent 9000, Belgium; Physics and Chemistry of Nanostructures, Ghent University, Gent 9000, Belgium; NOLIMITS Center for Non-Linear Microscopy and Spectroscopy, Gent 9000, Belgium;* orcid.org/0000-0001-9241-5585; Email: ivo.tanghe@ugent.be

Pieter Geiregat − *Physics and Chemistry of Nanostructures, Ghent University, Gent 9000, Belgium; NOLIMITS Center for Non-Linear Microscopy and Spectroscopy, Gent 9000, Belgium;* orcid.org/0000-0001-7217-8738; Email: pieter.geiregat@ugent.be

Authors

Tom Vandekerckhove − *Photonics Research Group, Ghent University, Gent 9000, Belgium;* orcid.org/0000-0002-5639-9300

Margarita Samoli − *Physics and Chemistry of Nanostructures, Ghent University, Gent 9000, Belgium;* orcid.org/0000-0003-0442-5420

Amelia Waters − *Department of Physics, Bowling Green State University, Bowling Green, Ohio 43403, United States*

Dulanjan Harankahage − *Department of Chemistry and The Center for Photochemical Sciences, Bowling Green State University, Bowling Green, Ohio 43403, United States*

Mikhail Zamkov − *The Center for Photochemical Sciences, Bowling Green State University, Bowling Green, Ohio 43403, United States; Department of Physics, Bowling Green State University, Bowling Green, Ohio 43403, United States;* orcid.org/0000-0002-8638-2972

Zeger Hens − *Physics and Chemistry of Nanostructures, Ghent University, Gent 9000, Belgium; NOLIMITS Center for Non-Linear Microscopy and Spectroscopy, Gent 9000, Belgium;* orcid.org/0000-0002-7041-3375

Christian Seassal − *Université Lyon, Ecole Centrale de Lyon, CNRS, INSA Lyon, Univ Claude Bernard Lyon 1, CPE Lyon, CNRS, INL, UMR5270, 69130 Ecully, France;* orcid.org/0000-0002-3856-9089

Hai-Son Nguyen − *Université Lyon, Ecole Centrale de Lyon, CNRS, INSA Lyon, Univ Claude Bernard Lyon 1, CPE Lyon, CNRS, INL, UMR5270, 69130 Ecully, France;* orcid.org/0000-0002-1638-2272

Dries Van Thourhout − *Photonics Research Group, Ghent University, Gent 9000, Belgium;* orcid.org/0000-0003-0111-431X

Complete contact information is available at: https://pubs.acs.org/10.1021/acsphotonics.4c01410

Funding

This work is partly supported by the French National Research Agency (ANR) under the project POLAROID (ANR-24-CE24-7616-01).

Notes

The authors declare no competing financial interest.

ACKNOWLEDGMENTS

I.T. acknowledges funding from IOF-STARTT Project "QD-LASER". M.S. acknowledges the SBO PROCEED project (no. S0002019N). The work of the Zamkov group was supported by the NSF award #2208834. A.W. acknowledges the support by DE-SC0016872 funded by the U.S. Department of Energy, Office of Science. P.G. acknowledges funding from the Research Foundation—Flanders (FWO-Vlaanderen under grant no. G037221N-HITEC) and the SBO PROCEED project (no. S0002019N) and the Core Facility program NOLIMITS at Ghent University. D.V.T. and Z.H. acknowledge funding through FWO (G0B2921N).

REFERENCES

(1) Ma, R.-M.; Oulton, R. F. Applications of nanolasers. *Nat. Nanotechnol.* **2019**, *14*, 12−22.

(2) Lu, X.; Chang, L.; Tran, M. A.; Komljenovic, T.; Bowers, J. E.; Srinivasan, K. Emerging integrated laser technologies in the visible and short near-infrared regimes. *Nat. Photonics* **2024**, *18*, 1010−1023.

(3) Liu, J.; Huang, G.; Wang, R. N.; He, J.; Raja, A. S.; Liu, T.; Engelsen, N. J.; Kippenberg, T. J. High-yield, wafer-scale fabrication of ultralow-loss, dispersion-engineered silicon nitride photonic circuits. *Nat. Commun.* **2021**, *12*, 2236.

(4) Chrostowski, L.; Hochberg, M. *Silicon Photonics Design: From Devices to Systems*; Cambridge University Press, 2015.

(5) Bogaerts, W.; De Heyn, P.; Van Vaerenbergh, T.; De Vos, K.; Kumar Selvaraja, S.; Claes, T.; Dumon, P.; Bienstman, P.; Van Thourhout, D.; Baets, R. Silicon microring resonators. *Laser Photon. Rev.* **2012**, *6*, 47−73.

(6) Xiang, C.; Guo, J.; Jin, W.; Wu, L.; Peters, J.; Xie, W.; Chang, L.; Shen, B.; Wang, H.; Yang, Q.-F.; et al. High-performance lasers for fully integrated silicon nitride photonics. *Nat. Commun.* **2021**, *12*, 6650.

(7) Roelkens, G.; Zhang, J.; Bogaert, L.; Soltanian, E.; Billet, M.; Uzun, A.; Pan, B.; Liu, Y.; Delli, E.; Wang, D.; et al. Present and future of micro-transfer printing for heterogeneous photonic integrated circuits. *APL Photonics* **2024**, *9*, 010901.

(8) Zhang, J.; Haq, B.; O'Callaghan, J.; Gocalinska, A.; Pelucchi, E.; Trindade, A. J.; Corbett, B.; Morthier, G.; Roelkens, G. Transfer-printing-based integration of a III-V-on-silicon distributed feedback laser. *Opt. Express* **2018**, *26*, 8821−8830.

(9) Vanackere, T.; Vandekerckhove, T.; Bogaert, L.; Billet, M.; Poelman, S.; Cuyvers, S.; Van Kerrebrouck, J.; Moerman, A.; Caytan, O.; Singh, N.; et al. Heterogeneous integration of a high-speed lithium niobate modulator on silicon nitride using micro-transfer printing. *APL Photonics* **2023**, *8*, 086102.

(10) Vandekerckhove, T.; Vanackere, T.; De Witte, J.; Lufungula, I. L.; Vissers, E.; Roelkens, G.; Clemmen, S.; Kuyken, B. High-efficiency second harmonic generation in heterogeneously-integrated periodically-poled lithium niobate on silicon nitride. In *European Conference on Lasers and Electro-Optics*, 2023.

(11) Sliz, R.; Lejay, M.; Fan, J. Z.; Choi, M.-J.; Kinge, S.; Hoogland, S.; Fabritius, T.; García de Arquer, F. P.; Sargent, E. H. Stable colloidal quantum dot inks enable inkjet-printed high-sensitivity infrared photodetectors. *ACS Nano* **2019**, *13*, 11988−11995.

(12) Yang, P.; Zhang, L.; Kang, D. J.; Strahl, R.; Kraus, T. High-resolution inkjet printing of quantum dot light-emitting microdiode arrays. *Adv. Opt. Mater.* **2020**, *8*, 1901429.

(13) Justo, Y.; Moreels, I.; Lambert, K.; Hens, Z. Langmuir−Blodgett monolayers of colloidal lead chalcogenide quantum dots: morphology and photoluminescence. *Nanotechnology* **2010**, *21*, 295606.

(14) Pang, C.; Deng, Y.-H.; Kheradmand, E.; Poonkottil, N.; Petit, R.; Elsinger, L.; Detavernier, C.; Geiregat, P.; Hens, Z.; Van Thourhout, D. Integrated PbS colloidal quantum dot photodiodes on silicon nitride waveguides. *ACS Photonics* **2023**, *10*, 4215−4224.

(15) Pang, C.; Deng, Y.-h.; Kheradmand, E.; Hagelsieb, L. M.; Guo, Y.; Cheyns, D.; Geiregat, P.; Hens, Z.; Van Thourhout, D. A silicon photonics waveguide-coupled colloidal quantum dot photodiode sensitive beyond 1.6 μm. *APL Photonics* **2024**, *9*, 066113.

(16) Van Avermaet, H.; Schiettecatte, P.; Hinz, S.; Giordano, L.; Ferrari, F.; Nayral, C.; Delpech, F.; Maultzsch, J.; Lange, H.; Hens, Z. Full-spectrum InP-based quantum dots with near-unity photoluminescence quantum efficiency. *ACS Nano* **2022**, *16*, 9701−9712.

(17) Moreels, I.; Justo, Y.; De Geyter, B.; Haustraete, K.; Martins, J. C.; Hens, Z. Size-tunable, bright, and stable PbS quantum dots: a surface chemistry study. *ACS Nano* **2011**, *5*, 2004−2012.
(18) Drijvers, E.; De Roo, J.; Geiregat, P.; Feher, K.; Hens, Z.; Aubert, T. Revisited wurtzite CdSe synthesis: a gateway for the versatile flash synthesis of multishell quantum dots and rods. *Chem. Mater.* **2016**, *28*, 7311−7323.
(19) Bisschop, S.; Geiregat, P.; Aubert, T.; Hens, Z. The impact of core/shell sizes on the optical gain characteristics of CdSe/CdS quantum dots. *ACS Nano* **2018**, *12*, 9011−9021.
(20) Tanghe, I.; Samoli, M.; Wagner, I.; Cayan, S. A.; Khan, A. H.; Chen, K.; Hodgkiss, J.; Moreels, I.; Thourhout, D. V.; Hens, Z.; et al. Optical gain and lasing from bulk cadmium sulfide nanocrystals through bandgap renormalization. *Nat. Nanotechnol.* **2023**, *18*, 1423−1429.
(21) Tanghe, I.; Molkens, K.; Vandekerckhove, T.; Respekta, D.; Waters, A.; Huang, J.; Beavon, J.; Harankahage, D.; Lin, C. Y.; Chen, K.; et al. Two-dimensional electron−hole plasma in colloidal quantum shells enables integrated lasing continuously tunable in the red spectrum. *ACS Nano* **2024**, *18*, 14661−14671.
(22) Zhu, Y.; Xie, W.; Bisschop, S.; Aubert, T.; Brainis, E.; Geiregat, P.; Hens, Z.; Van Thourhout, D. On-chip single-mode distributed feedback colloidal quantum dot laser under nanosecond pumping. *ACS Photonics* **2017**, *4*, 2446−2452.
(23) Xie, W.; Stöferle, T.; Raino, G.; Aubert, T.; Bisschop, S.; Zhu, Y.; Mahrt, R. F.; Geiregat, P.; Brainis, E.; Hens, Z.; et al. On-chip integrated quantum-dot−silicon-nitride microdisk lasers. *Adv. Mater.* **2017**, *29*, 1604866.
(24) Ahn, N.; Park, Y.-S.; Livache, C.; Du, J.; Gungor, K.; Kim, J.; Klimov, V. I. Optically excited lasing in a cavity-based, high-current-density quantum dot electroluminescent device. *Adv. Mater.* **2023**, *35*, 2206613.
(25) Ahn, N.; Livache, C.; Pinchetti, V.; Jung, H.; Jin, H.; Hahm, D.; Park, Y.-S.; Klimov, V. I. Electrically driven amplified spontaneous emission from colloidal quantum dots. *Nature* **2023**, *617*, 79−85.
(26) Taghipour, N.; Dalmases, M.; Whitworth, G. L.; Dosil, M.; Othonos, A.; Christodoulou, S.; Liga, S. M.; Konstantatos, G. Colloidal quantum dot infrared lasers featuring sub-single-exciton threshold and very high gain. *Adv. Mater.* **2023**, *35*, 2207678.
(27) Adachi, M. M.; Fan, F.; Sellan, D. P.; Hoogland, S.; Voznyy, O.; Houtepen, A. J.; Parrish, K. D.; Kanjanaboos, P.; Malen, J. A.; Sargent, E. H. Microsecond-sustained lasing from colloidal quantum dot solids. *Nat. Commun.* **2015**, *6*, 8694.
(28) Fan, F.; Voznyy, O.; Sabatini, R. P.; Bicanic, K. T.; Adachi, M. M.; McBride, J. R.; Reid, K. R.; Park, Y.-S.; Li, X.; Jain, A.; et al. Continuous-wave lasing in colloidal quantum dot solids enabled by facet-selective epitaxy. *Nature* **2017**, *544*, 75−79.
(29) Akahane, Y.; Asano, T.; Song, B.-S.; Noda, S. High-Q photonic nanocavity in a two-dimensional photonic crystal. *Nature* **2003**, *425*, 944−947.
(30) Emoto, K.; Koizumi, T.; Hirose, M.; Jutori, M.; Inoue, T.; Ishizaki, K.; De Zoysa, M.; Togawa, H.; Noda, S. Wide-bandgap GaN-based watt-class photonic-crystal lasers. *Commun. Mater.* **2022**, *3*, 72.
(31) Inoue, T.; Yoshida, M.; Zoysa, M.; Ishizaki, K.; Noda, S. Design of photonic-crystal surface-emitting lasers with enhanced in-plane optical feedback for high-speed operation. *Opt. Express* **2020**, *28*, 5050−5057.
(32) Joannopoulos, J. D.; Johnson, S. G.; Winn, J. N.; Meade, R. D. *Molding the Flow of Light*; Princeton University Press, 2008; Vol. *12*.
(33) Cassidy, J.; Diroll, B. T.; Mondal, N.; Berkinsky, D. B.; Zhao, K.; Harankahage, D.; Porotnikov, D.; Gately, R.; Khon, D.; Proppe, A.; Bawendi, M. G.; et al. Quantum shells boost the optical gain of lasing media. *ACS Nano* **2022**, *16*, 3017−3026.
(34) Harankahage, D.; Cassidy, J.; Beavon, J.; Huang, J.; Brown, N.; Berkinsky, D. B.; Marder, A.; Kayira, B.; Montemurri, M.; Anzenbacher, P.; et al. Quantum shell in a shell: engineering colloidal nanocrystals for a high-intensity excitation regime. *J. Am. Chem. Soc.* **2023**, *145*, 13326−13334.
(35) Sakai, K.; Miyai, E.; Sakaguchi, T.; Ohnishi, D.; Okano, T.; Noda, S. Lasing band-edge identification for a surface-emitting photonic crystal laser. *IEEE J. Sel. Area. Commun.* **2005**, *23*, 1335−1340.
(36) Cueff, S.; Berguiga, L.; Nguyen, H. S. Fourier imaging for nanophotonics. *Nanophotonics* **2024**, *13*, 841−858.
(37) Noda, S.; Kitamura, K.; Okino, T.; Yasuda, D.; Tanaka, Y. Photonic-crystal surface-emitting lasers: review and introduction of modulated-photonic crystals. *IEEE J. Sel. Top. Quantum Electron.* **2017**, *23*, 1−7.
(38) Kodigala, A.; Lepetit, T.; Gu, Q.; Bahari, B.; Fainman, Y.; Kanté, B. Lasing action from photonic bound states in continuum. *Nature* **2017**, *541*, 196−199.
(39) Wu, M.; Ha, S. T.; Shendre, S.; Durmusoglu, E. G.; Koh, W.-K.; Abujetas, D. R.; Sánchez-Gil, J. A.; Paniagua-Domínguez, R.; Demir, H. V.; Kuznetsov, A. I. Room-temperature lasing in colloidal nanoplatelets via Mie-resonant bound states in the continuum. *Nano Lett.* **2020**, *20*, 6005−6011.
(40) Chen, L.; Lopez-Garcia, M.; Taverne, M. P.; Zheng, X.; Ho, Y.-L. D.; Rarity, J. Direct wide-angle measurement of a photonic band structure in a three-dimensional photonic crystal using infrared Fourier imaging spectroscopy. *Opt. Lett.* **2017**, *42*, 1584−1587.
(41) Le Thomas, N.; Houdré, R.; Kotlyar, M. V.; O'Brien, D.; Krauss, T. F. Exploring light propagating in photonic crystals with Fourier optics. *J. Opt. Soc. Am. B* **2007**, *24*, 2964−2971.
(42) Amemiya, T.; Okada, S.; Kagami, H.; Nishiyama, N.; Yao, Y.; Sakoda, K.; Hu, X. High-speed infrared photonic band microscope using hyperspectral Fourier image spectroscopy. *Opt. Lett.* **2022**, *47*, 2430−2433.
(43) Yokoyama, M.; Noda, S. Finite-difference time-domain simulation of two-dimensional photonic crystal surface-emitting laser. *Opt. Express* **2005**, *13*, 2869−2880.
(44) Asano, T.; Ochi, Y.; Takahashi, Y.; Kishimoto, K.; Noda, S. Photonic crystal nanocavity with a Q factor exceeding eleven million. *Opt. Express* **2017**, *25*, 1769−1777.

https://doi.org/10.1021/acsphotonics.4c01410
ACS Photonics 2024, 11, 4906−4915